Topology Optimization of Lattice Support Structure for Cantilever Beams Fabricated Via Laser Powder Bed Fusion

Jiazheng Hu, Marjan Molavi-Zarandi, and Damiano Pasini*

Herein, a numerical scheme is presented to design, optimize, generate, and manufacture a lattice support structure that reduces thermal-induced distortion in metallic components 3D printed by laser powder bed fusion (LPBF). The inherent strain method is implemented in the framework to fast predict the part distortion during an LPBF build, and asymptotic homogenization is used to determine the effective properties of the lattice support with a triply periodic minimum surface topology. The framework is tested on a practical case study that involves the design of the optimized gradient of a lattice that supports a cantilever beam and compares the results with benchmark designs, a lattice support structure with uniform relative density and a fully solid support. The optimized support can reduce the distortion pattern throughout the entire cantilever beam and reduces the beam tip distortion of 69% and 58% in comparison to the uniform lattice and fully solid support. To demonstrate the viability of the design workflow here presented, a proof-of-concept lattice support is manufactured out SS316 stainless steel via LPBF.

1. Introduction

Additive manufacturing (AM) is a well-established process for building components with a fairly intricate architecture.[1–4] In the realm of metal 3D printing, layers of material powder are typically melted and solidified in a powder bed layer-by-layer to form a 3D object. For processes that involve a laser powder bed fusion (LPBF), the laser beam generates an intense heat flux among adjacent layers, typically causing thermal deformation and residual stresses. A common approach to compensate for excessive part deformation due to residual stress is to introduce

J. Hu, D. Pasini
Department of Mechanical Engineering
McGill University
Montreal, Quebec H3A 0C3, Canada
E-mail: damiano.pasini@mcgill.ca

M. Molavi-Zarandi
National Research Council Canada (NRC)
Automotive and Surface Transportation Research Center
Numerical Simulation Group
Boucherville, QC J4B 6Y4, Canada

The ORCID identification number(s) for the author(s) of this article can be found under https://doi.org/10.1002/adem.202300976.

a rigid structure, namely a support structure, that shoulders the object being printed. A support structure is commonly required to prevent sagging or collapse if the object to print contains attributes inclined at an angle above 45° with respect to the building plane.[5]

Support structures are well established means to address problems associated with part overhang and distortion, as well as stability and dimensional accuracy. Yet, they still pose a number of challenges. First, the post-processing operation required for the support removal from a 3D printed component can be cumbersome and error-prone.[6,7] Second, the excessive volume generated by the sacrificial support significantly increases material consumption, hence lowering the overall process efficiency.[8] One way to address these challenges is to resort to optimization strategies that seek a balanced trade-off between the maximization of the benefits delivered by a support structure and the minimization of its additional cost.

Methods for reducing the need for a support structure can be loosely categorized into two mainstreams. The first aims at avoiding any modification to the 3D printed object through either part reorientation only[9–11] or support optimization for a given field. It is well known the 3D printing direction influences the geometric accuracy and mechanical properties of the 3D printed part. Hence, relying solely on the manipulation of part orientation is not always the best strategy to reduce the emergence of manufacturing imperfections.[12] The second uses structural optimization or feature-based methods to act also on the design of the original object, mainly through modification of its original geometry, so as to minimize the need for its support while attempting to minimize possible changes that might alter its original functions.[13–17]

This work falls in the first category that avoids part modification and seeks the optimal structural support for the overall reduction of material cost and part distortion. Within this category, existing works that focus on the design of a support structure for an optimal field response have so far considered two fields, either thermal or/and displacement. For the first, the thermal field drives the optimization process to find the optimal material distribution of the support structure. For example, a transient thermal analysis was incorporated into a topology optimization framework to minimize the temperature difference between the printing bed and selected points across the design domain.[18] In another approach, the results from a layer-wise

transient thermal analysis were converted into an aggregate equivalent static load. A thermal compliance optimization problem was then formulated to find the optimal tree-like support structure.[7] More recently, an analytical model was proposed to determine the transient heat conduction for a given volume flux. A level-set-based topology optimization framework was developed to maximize the heat dissipation capacity of solid support.[19]

The second set of existing works for structure support optimization use displacement and stress fields, as opposed to the thermal field (see **Table 1** for a brief summary). The reason to bypass a thermal analysis is that during the LPBF process, the metal powder undergoes complex phase transitions that can be modeled with multiphysics analysis, but they are computationally expensive to use if several iterations are required to reach a solution, such as in structural optimization. Hence, simplified yet sufficiently accurate mechanical models become handy for part-scale analysis. For example, an equivalent static load was derived from a previously developed transient thermal-mechanical model and then used in a compliance minimization problem.[20] Body forces originating from both the self-weight and the inherent strain were combined and included in the compliance minimization formulation to generate an optimal solid support structure with inferior deformation at the tip of the cantilever beam. The analytical model therein proposed demonstrates that a stiffer support structure reduces part deflection, thus corroborating the choice compliance minimization as an objective function.[21] In another work, on the other hand, the inherent strain method (ISM) was used to fast predict the residual stress distribution in the part. The inherent strain value was determined via a micro-scale thermal-mechanical analysis and then used to design a graded lattice support at minimum mass and under stress constraint.[22] An experimentally determined inherent stain value was used in a part-scale model, and the density gradient of the lattice support structure was optimized to limit the layer-by-layer vertical displacement during LPBF.[23] A calibration-based structural approach was also utilized to quantify the residual stress and distortion during the AM process, and a compliance minimization problem was formulated by converting the maximum recorded von Mises stress at forty inspection points across the domain into their corresponding load magnitude.[24]

Herein, a topology optimization framework is proposed to design a lattice support structure for LPBF. We use an inherent strain vector to fast predict the part distortion at the final stage of

the AM build. Asymptotic homogenization (AH) along with appropriate property scaling laws are used to calculate the effective properties of the lattice support at the part-scale model. A compliance minimization problem is formulated to solve for the optimal density distribution of the lattice support with a prescribed cell topology, e.g., triply periodic minimal surface (TPMS). Both the topology optimization and numerical simulation are conducted via in-house MATLAB (The Math Works, Inc., USA) codes. The results, mainly the deflection, are contrasted with those from benchmark counterparts, i.e., a fully solid support and a uniform density lattice. The three candidate support structures are manufactured and qualitatively assessed.

2. Results and Discussion

2.1. Design Domain and Workflow

Double cantilever T-beams, U-shape tubes, and L-shape cantilevers are typically used (see Table 1) to benchmark the process-induced distortion caused by metal AM. In particular, cantilever beams are widely used to design actuation and sensing mechanisms in miniaturized systems[25]. In this study, an L-shape cantilever constrained at the short end (**Figure 1**) is selected due to its simple yet commonly used geometry. As the cantilever is fixed at one end, the thermal-induced distortion is restrained at the base, then accumulates and propagates along its overhang. This generates a distortion pattern with maximum displacement at
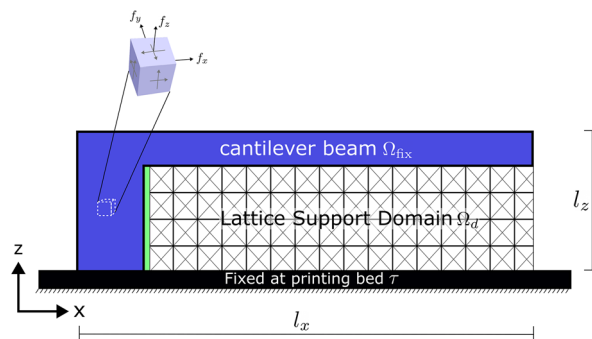

Figure 1. Design domain of lattice support structure for cantilever beam. Both cantilever beam (Ω_{fix}) and lattice support (Ω_{d}) restrained at printing bed τ; and Ω_{fix} subjected to body force f_{xyz}.

Table 1. Summary of main approaches that use a displacement and stress field to design the optimal support structure for metal AM.

Author	Type of support	Objective and constraints	Method of field analysis
Allaire et al.[20]	Solid	Compliance minimization with a volume constraint	Convert the results of a transient thermal mechanical analysis into an equivalent static force
Zhang et al.[21]	Solid	Compliance minimization with a volume constraint	Inherent strain method with parallel computing
Cheng et al.[22]	Cubic thin-wall lattice	Mass minimization with stress constraint	Inherent strain method
Pellens et al.[23]	Iso-truss lattice	Mass minimization with layer-wise displacement control	Inherent strain method measured from experiments
Bartsch et al.[24]	Solid	Compliance minimization with a volume constraint	Calibration-based structural approach offered by a commercial package

the tip of the cantilever, a metric that we can use to measure the effectiveness of a given type of support.

Figure 1 illustrates the design domain (Ω) for our structural support shouldering a cantilever beam (length l_x, width l_y, and height along the building direction (z) l_z). The cantilever beam (Ω_{fix}) is prescribed, and only the lattice support is our design domain (Ω_d). Both the Ω_{fix} and Ω_d are restrained at the printing bed τ. A gap (green) along the z direction is left between Ω_d and Ω_{fix} to visually distinguish the two domains. Inherent strain-induced body forces f_{xyz} are applied to the elements in Ω_{fix}. **Figure 2** shows the general workflow of our lattice design framework, where each step is detailed in the following sections.

2.2. Inherent Strain Method

Originally developed to predict process-induced residual stress in welded parts, the ISM has become a viable and efficient approach to predict part distortion emerging during AM process.[26] ISM is essentially a multiscale approach where a transient thermal-mechanical coupled model is only carried out at the micro-scale for a representative scanning pattern.[27] An inherent strain vector ε^{inh} is extracted from the steady state of the micro-scale simulation. ε^{inh} represents the prominent feature of the ISM, as it can be used to expedite the part-scale structural analysis when used in topology optimization. This enables to skip the lengthy process to find a solution for a fully coupled model at each iteration.

ε^{inh} is used in the part-scale structural analysis to calculate the ith element body force $f_i^{(e)}$, where the expression of $f_i^{(e)}$ is derived from the strain-displacement matrix ($B^{(e)}$) and constitutive matrix ($D^{(e)}$) of the elastic constants as

$$f_i^{(e)} = \int_{\Omega^{(e)}} B_i^{\text{T}(e)} D_i^{(e)} \varepsilon^{\text{inh}} d\Omega_i^{(e)} \tag{1}$$

To better compare our support structure design with those obtained with existing topology optimization that uses the displacement field, we use experimentally measured values for the inherent strain vector.[23] The body forces $f_i^{(e)}$ derived from the inherent strain vector are calculated for the elements of the cantilever beam only, excluding those of the support domain, making the inherent strain-induced forces independent from the design variables of the lattice support.

2.3. Asymptotic Homogenization

To optimize the property gradients of the lattice support for minimum compliance, the elastic properties of the selected lattice should be available. A fully resolved finite element model that contains the detailed attributes of every lattice cell is computationally prohibitive. For this reason, we resort to the effective properties of a representative volume element (RVE) at the part-scale model, and resort to AH,[28,29] a homogenization
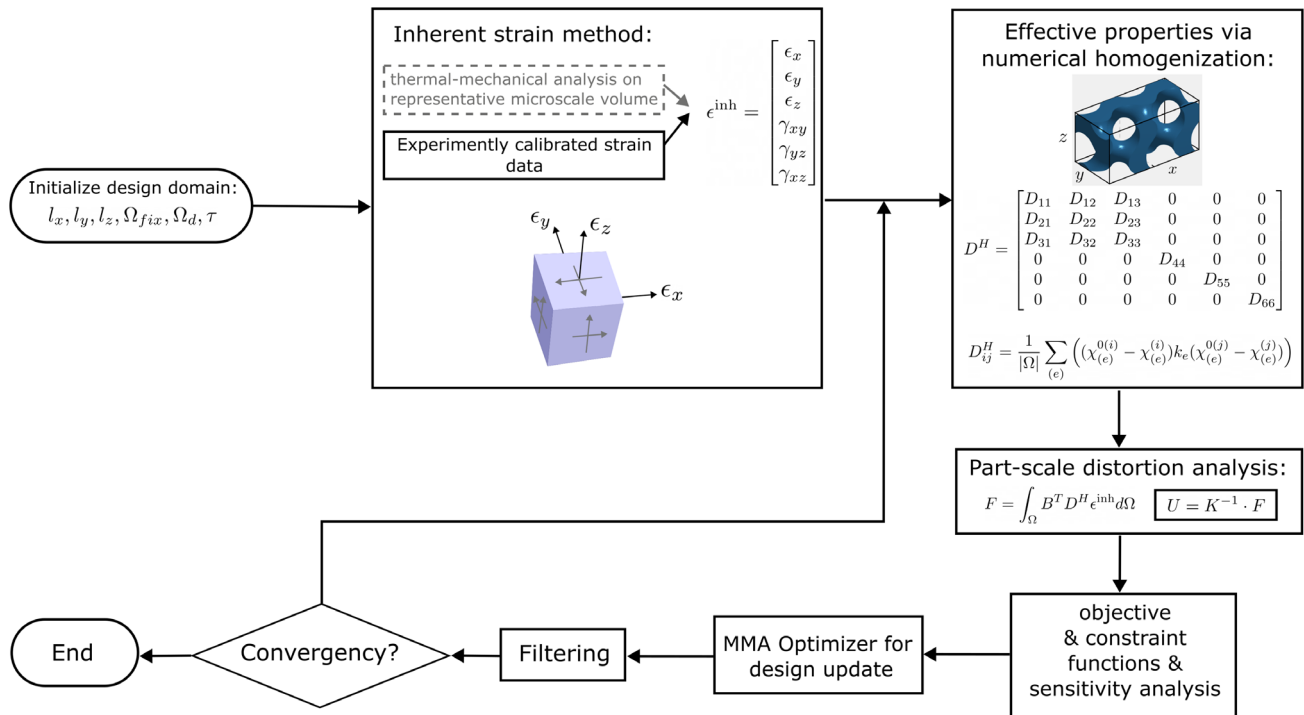

Figure 2. General workflow of the lattice support design. a) Initialization of the design domain; b) Extraction of the inherent strain vector, used to calculate the body force in the part-scale analysis; c) Effective properties of the selected unit cell via numerical homogenization; d) Part-scale structural analysis to compute the displacement field; e) Determination of objective function values and constraint functions and evaluation of gradient through sensitivity analysis; f) Update of design variables based on sensitivity analysis where MMA stands for method of moving asymptotes; g) Application of a density filter to mitigate numerical artifacts.

theory that enables to calculate the effective properties of the RVE, in this case, the unit cell of a periodic lattice.

As per the cell topology, we select a Gyroid lattice, a TPMS. This choice is motivated by the multiphysical properties a TPMS offers in the context of metal AM process:[30–34] 1) self-standing, i.e., TPMS no longer needs support to shoulder it; 2) continuous shell-based surface enabling a more uniform stress distribution; 3) high specific surface area-to-volume ratio, which provides a better thermal dissipation capacity than conventional truss-based lattices.

The homogenized compliance matrix D_{ij}^{H} of a Gyroid TPMS lattice is calculated by the following equation

$$D_{ij}^{\mathrm{H}} = \frac{1}{|\mathbf{\Omega}|} \sum_{(e)} \int_{\Omega^{(e)}} \left(\left(\chi_{0(i)}^{(e)} - \chi_{(i)}^{(e)} \right) k^{(e)} \left(\chi_{0(j)}^{(e)} - \chi_{(j)}^{(e)} \right) \right) d\Omega^{(e)} \tag{2}$$

where $\chi_{0(i)}^{(e)}$ is the element displacement field corresponding to the ith unit strain. $\chi_{(i)}^{(e)}$ is the displacement field calculated from the global stiffness equation. $\Omega^{(e)}$ is the total area or volume of a prescribed unit cell. Gyroid TPMS lattices have cubic symmetry,[35,36] which reduces the number of independent elastic constants to three, i.e., D_{11}, D_{12}, D_{44} such as

$$D_{ij}^{\mathrm{H}} = \begin{bmatrix} D_{11} & D_{12} & D_{12} & 0 & 0 & 0 \\ D_{12} & D_{11} & D_{12} & 0 & 0 & 0 \\ D_{12} & D_{12} & D_{11} & 0 & 0 & 0 \\ 0 & 0 & 0 & D_{44} & 0 & 0 \\ 0 & 0 & 0 & 0 & D_{44} & 0 \\ 0 & 0 & 0 & 0 & 0 & D_{44} \end{bmatrix} \tag{3}$$

Given the existence of scaling laws for the elastic properties of several TPMS-based lattices including Gyroid,[32] the relation between homogenized elasticity constants (D_{ij}^{H}), elasticity constants of the solid material (D_{ij}^{*}), and the relative density ($\rho^{(e)}$) of the unit cell are given by

$$\begin{cases} D_{11} = D_{11}^{*} \left(0.0605 e^{2.8659 \rho^{(e)}} - 0.0605 \right) \\ D_{12} = D_{12}^{*} \left(0.0396 e^{3.2513 \rho^{(e)}} - 0.0396 \right) \\ D_{44} = D_{44}^{*} \left(0.1452 e^{2.0729 \rho^{(e)}} - 0.1452 \right) \end{cases} \tag{4}$$

Several recent studies have reported correlations among the lattice topology, the relative density of the unit cell, and the inherent strain value,[37] meaning that both the inherent strain value and the effective property depend on the topology of the unit cell printed via LPBF and its relative density. In this work, however, only the relation between relative density and effective properties is considered.

2.4. Topology Optimization of Lattice Support

Among existing approaches for topology optimization, such as density-based,[38–41] level-set,[42–45] and other differential equation-driven approaches,[46–50] in this work we use a density-based method. The design domain Ω shown in Figure 1

comprises a solid cantilever beam Ω_{fix} and a lattice support domain Ω_{d}. Both Ω_{fix} and Ω_{d} are discretized into voxel elements where each element e in Ω is assigned a density variable ρ_e ($0 < \rho_e \leq 1$), representing the relative density of each voxel, i.e., zero density for void, one for solid. Ω_{fix} is prescribed with a cantilever geometry, thus ρ_e has value of 1 for all e within the domain, whereas ρ_e within Ω_{d} are updated iteratively during the optimization process.

Our goal here is to maximize the stiffness of the lattice support so as to minimize the distortion of the 3D printed part. This is formulated in terms of compliance, i.e., we minimize the compliance (C) of the design domain Ω as

$$\begin{cases} \min_{\rho_e} : & C = F_{\mathrm{inh}}^{\mathrm{T}} U(\rho_e), \quad \forall e \in \Omega \\ \\ s.t. & \begin{cases} K(D^{\mathrm{H}}(\rho_e)) U(\rho_e) = F_{\mathrm{inh}} \\ \sum_{i=1}^{N_{\mathrm{nele}}} \rho_e v_0 - V_{\mathrm{lim}} \leq 0 \\ 0.15 \leq \rho_e \leq 0.85, \quad e = 1, 2, \dots N_{\mathrm{nele}} \end{cases} \end{cases} \tag{5}$$

where U is the global nodal displacements of all degrees of freedom, and F_{inh} is the body force calculated through the inherent strain vector. The first equation of the equality constraint is the state function where $K(D^{\mathrm{H}}(\rho_i))$ is the global stiffness matrix assembled using homogenized effective properties. (See Supporting Information for more details about the integration of the inherent strain vector into the topology optimization framework, as well as the sensitivity analysis.) The second inequality constraint ensures that the total volume of the lattice support does not exceed the prescribed limit V_{lim} where v_0 represents the unit volume of a voxel element. The last line is a bound constraint for the design variables ρ_i. It sets the physical lower and upper bounds of the lattice relative density not exceeding 15% and 85%; in particular, it ensures the element connectivity for shell-based lattices with low density and prevents powder entrapping due to void closure at high volume fraction[51]

A gradient-based optimizer that is widely adopted for large-scale structural design problems, the method of moving asymptotes (MMA),[52] is used to find the optimum solution. For a faster convergence, we analytically derive the close-form expressions of the partial derivatives of both the objective and constraint functions w.r.t. the design variables, i.e., the sensitivity analysis. By using the chain rule and the adjoint method, the results of the sensitivity analysis can be expressed as

$$\frac{\partial C}{\partial \rho_i} = -p \rho_i^{(p-1)} (E_0 - E_{\mathrm{min}}) u_i^T k_0 u_i \tag{6}$$

$$\frac{\partial V}{\partial \rho_i} = v_{\mathrm{s}} \tag{7}$$

where v_{s} is the volume of the solid element, p is the coefficient introduced in the solid isotropic material with penalization (SIMP) method[40] to ensure a black-and-white solution. Typically, a value of 3 is proved to be an optimal choice of p if one seeks for a black-and-white solution. In this work dealing with lattice materials, however, p is assigned the value of 1 to enable a smooth transition between regions of intermediate density (see Supporting Information for the analysis on the role

**ADVANCED
SCIENCE NEWS**

www.advancedsciencenews.com

**ADVANCED
ENGINEERING
MATERIALS**

www.aem-journal.com

of the penalty factor p (1 versus 3) in a Gyroid lattice). E_0 is the stiffness of solid material and E_{min} is a very small value assigned to the void element. The concept of E_0 and E_{min} is first introduced in the modified SIMP method with a number of advantages compared to the original formulation.[53] The sensitivity calculation of the volume constraint assumes that all voxel elements have a unit volume and remain in the linear elastic regime.

To ensure the existence of the solution and avoid numerical artifacts, e.g., the formation of checkerboard patterns, we apply a density filter to both the sensitivities and design variables. We use a very adaptive density filter that can be predetermined before the optimization,[54] where the filtered element density $\tilde{\rho}_e$ is used in lieu of the original counterpart ρ_e during the optimization process. As a result, we first derive the sensitivities with respect to the density variable ρ_i for the *ith* element by means of the chain rule

$$\tilde{\rho}_i = \frac{1}{\sum_{j \in N_{nele}} H_{ji}} \sum_{j \in N_{nele}} H_{ji} \rho_i \tag{8}$$

$$\frac{\partial \Phi}{\partial \rho} = \frac{\partial \Phi}{\partial \tilde{\rho}} \frac{\partial \tilde{\rho}}{\partial \rho} \tag{9}$$

where $\tilde{\rho}_i$ is the filtered density for the *ith* element. H_{ji} is the spatial linear operator that calculates the center-to-center distance from element i to all its neighboring elements j, and Φ represents either the objective or constraint function.

Figure 3 illustrates the result of the TPMS lattice support along with the design of two benchmark supports, a lattice support with a uniform relative density of 35%, and a fully solid support. The 2D cantilever beam has a dimension of 80 mm in length (l_x) and is 20 mm tall (l_z) along the printing direction z. The subdesign domain Ω_d for the lattice support structure has a dimension of 70 mm × 18 mm. The printing distortion with the

optimal lattice support is illustrated in Figure 3a, whereas (b) and (c) present the distortion of the uniform lattice support and solid support.

In Figure 3c, the most severe deformation values are observed at the top left and right corners, measured at 0.30 and 0.27 mm, respectively. Cantilever beams with uniform lattice support (b) and graded lattice support (a) both preserve the general trend observed in (c), i.e., the distortion increases from the center to either end. The optimally graded Gyroid support exhibits the most uniform distortion pattern among the three designs. The beam with the uniform lattice support (b), however, has the greatest absolute tip deformation observed (0.37 mm). For the prescribed body force, the uniform lattice with a volume fraction of 35% deforms more severely than the solid support structure. This is partially due to the decrease in the overall stiffness due to the mass reduction we observe from the solid (c) to the lattice material (b). For the prescribed volume fraction in (b), the cantilever beam with the optimized Gyroid lattice in (a) shows improved control over the absolute tip distortion, e.g., left 0.09 mm and right 0.11 mm. The overhang tip deformation decreases by 58% with respect to the solid support and 69% from the uniform lattice support.

The earlier results serve to benchmark the performance of the optimized support with the Gyroid lattice with that of a support with a uniform lattice, and one with a fully solid material. The distortion pattern and ultimate tip deflection of the Gyroid lattice support far outpace those of the uniform and solid supports. In addition, the results shown in Figure 3 resemble the density distribution previously found for the optimal support configuration,[23] i.e., the high-density regions propagate both diagonally and vertically from the cantilever tip to the printing bed. Despite the similarity, we note that in the literature, a layer-wise displacement-controlled formulation was used to generate an iso-truss lattice structure as opposed to the one
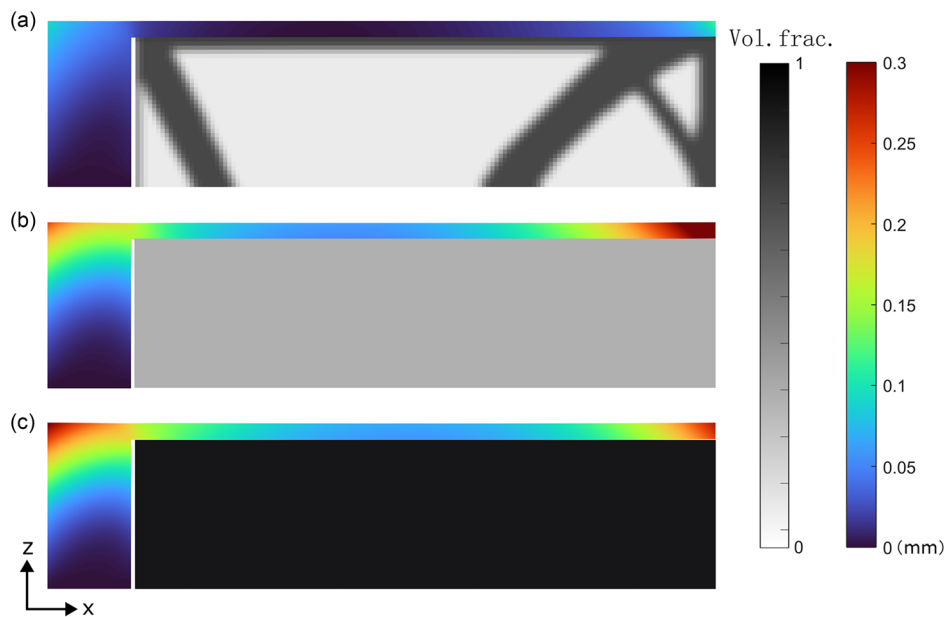

Figure 3. Displacement fields for a) a Gyroid TPMS lattice support structure with optimal density distribution; b) a Gyroid TPMS lattice support structure with uniform density; c) a solid support structure. A total volume fraction of 35% is maintained in both (a) and (b).

**ADVANCED
SCIENCE NEWS**

www.advancedsciencenews.com

**ADVANCED
ENGINEERING
MATERIALS**

www.aem-journal.com

adopted in this work. To further demonstrate the improvement our numerical scheme can generate, we compare in Figure S1, Supporting Information, the performance of a support consisting of our optimized Gyroid lattice with that made of an iso-truss lattice, used as a benchmark. The distribution of the distortion pattern and ultimate tip deformation of the former are superior to those of the latter. In particular, the maximum overhang tip deformation of the iso-truss lattice (Figure S1b, Supporting Information) is 50% (0.22 mm) above that of the Gyroid-based lattice support (Figure S1a, Supporting Information), hence showing the advantages of using a Gyroid-based lattice.

Figure 4 shows 3D renderings of an AM-enabled model with a total allowable support volume fraction of 25%. The volumetric density distribution in Figure 4a comprises section cuts along both the longitudinal (x) and transverse (y) directions. To unveil the internal density distribution of the topology optimized lattice support, section cuts in the format of those shown in Figure 3 are illustrated in Figure 4b at six representative locations, i.e., two cuts along x (S1 & S2) and four cuts along y (A1–A4). The results in Section S1 and S2, show dense regions originating from both top corners and diagonally propagating to the base plate. At the cantilever

tips, the general directions of the dense region revert from those shown in S1 and S2, although the displacement fields at section cuts along the longitudinal direction parallel the results of the 2D case, i.e., the distortion increases from the center to either end. Combining A4, S1, and S2, the density variation along the transverse direction observed in A4 enables to gain insights into the transition of the diagonally inverted dense regions from S1 to S2.

The cantilever beams with different support configurations are fabricated by LPBF (Renishaw AM-400, Renishaw Ltd., UK) using SS316 steel powder. **Figure 5**a shows from top to bottom the resultant cantilever beams with uniform lattice support, optimal lattice support, and solid support, respectively. Due to the symmetry, three transparent section cuts are created and shaded in sequence to illustrate the 3D internal structure of the cantilever beam support with optimal density distribution (Figure 5b). The transparent section cuts at the top and bottom of Figure 5b, respectively, resemble the sectional density distribution shown in S2 and S1 from Figure 4b, i.e., high-density lattice cells are diagonally constructed from the cantilever tips to the base, while the propagating directions are reversed at different cuts.
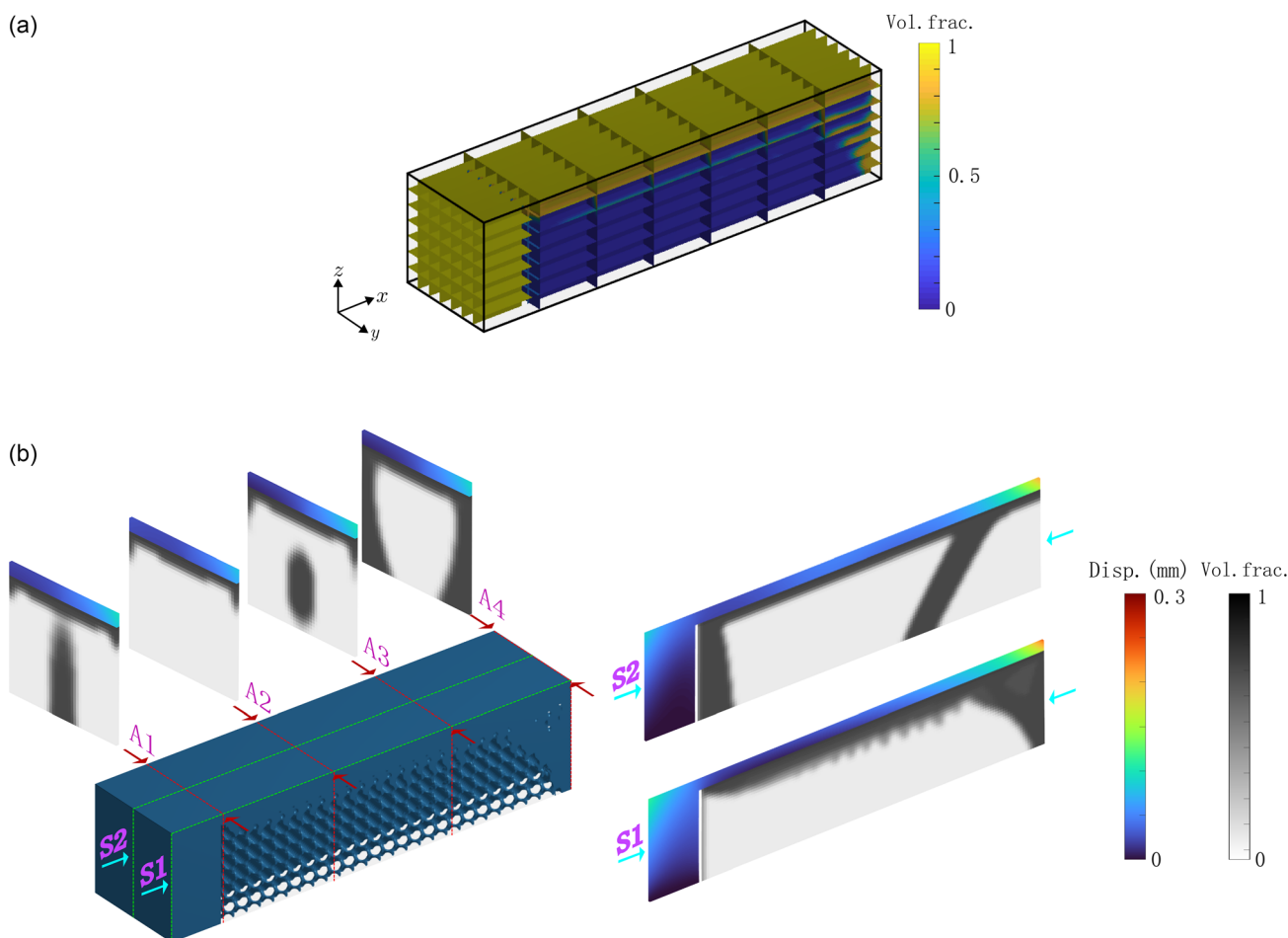

Figure 4. Volume fraction and 3D rendering model. a) Spatial volume fraction composed of density distribution at representative cross sections. b) 3D rendering cantilever beams with optimal Gyroid support structure. Displacement fields and density distributions are given at several representative cross sections. The periodic Gyroid lattice structure is generated using the open-source package Flatt_Pack.[51]
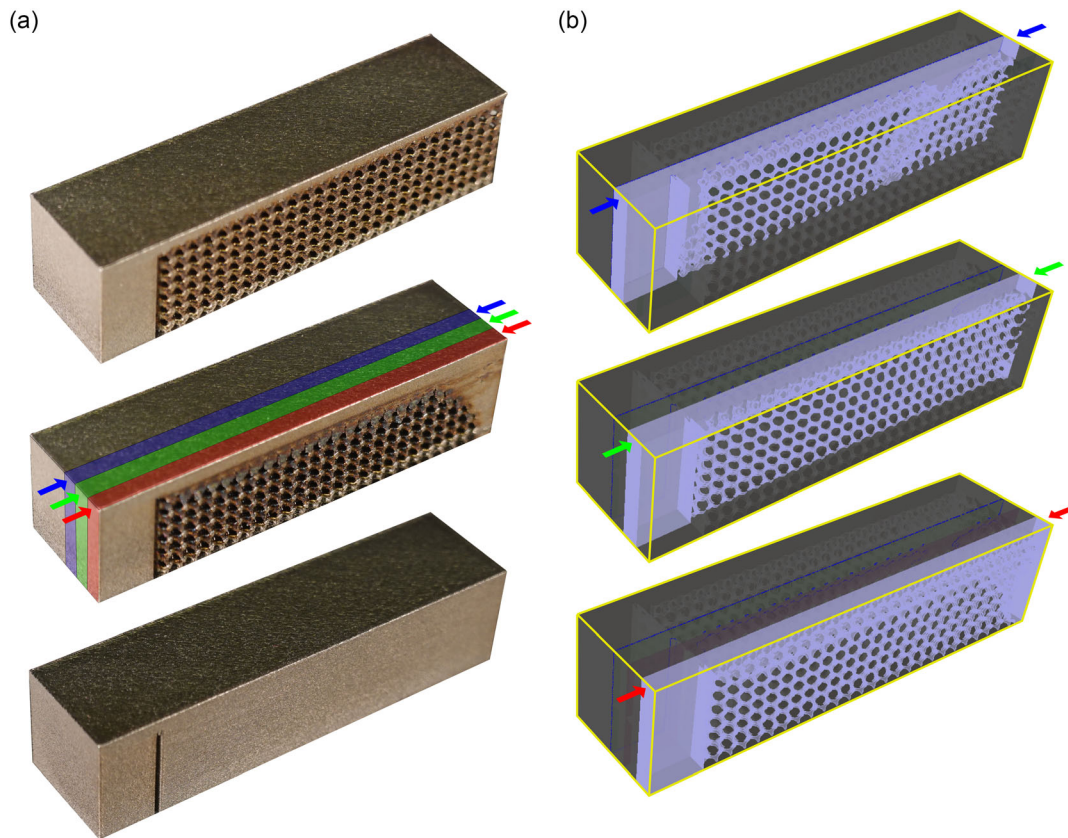
**ADVANCED
SCIENCE NEWS**

www.advancedsciencenews.com

**ADVANCED
ENGINEERING
MATERIALS**

www.aem-journal.com

Figure 5. a) Additive manufactured cantilever beams with given support configurations. From top to bottom, cantilever beams with uniform lattice support, optimal lattice support, and solid support. Overall dimension of cantilever beams: 60 mm × 15 mm × 15 mm. Describe here again what you have from top to bottom. b) Sequentially illuminated section views revealing the internal structure at the given longitudinal section of the beam with optimized lattice support shown in the middle position of (a).

3. Conclusions, Limitations, and Outlook

This study has presented a numerical scheme to design, optimize, and generate lattice support structure that reduces part distortion during the LPBF process. An inherent strain vector has been leveraged in the part-scale model to fast determine the displacement field at the final step of the printing stage. The topology optimization framework is applied to design a lattice support with a Gyroid topology. The density distribution obtained through topology optimization is mapped into to a discrete lattice support before fabrication via LPBF. The as-built cantilever beams are qualitatively validated and compared to other baseline supports. One key result of this work is that the optimized Gyroid lattice can better reduce the tip distortion of the supported cantilever than that attained by an iso-truss-based lattice. 1) The Gyroid lattice support with optimized density distribution smears the distortion pattern, leaving a more uniform displacement field across the entire domain with respect to cantilever beams with either a solid support or uniform lattice support. 2) The optimal lattice support reduces the tip deformation with respect to the cantilever beams with solid support, i.e., a 58% decrease in tip deformation. 3) The optimized redistribution

of the support material at 35% volume fraction and with no extra addition reduces 69% the cantilever tip deformation from the beam supported by a uniform lattice. 4) The Gyroid lattice outpaces the iso-truss lattice, selected as a benchmark of a strut-based cellular material, for the support of the cantilever beam.

While the present study has focused on the lattice support design for LPBF, there are a number of limitations that we summarize later, offering directions for future research: 1) The inherent strain vector adopted in this work needs to be experimentally validated for the cell topology here selected. Future work is required to develop a method that can precisely predict the inherent strain value for a certain cell topology. 2) A quantitative assessment of part distortion should be carried out to consolidate the numerical method proposed in this work. Part removal from the lattice support is to be done through wire electrical discharge machining so as to ensure smooth separation between them. A possible route to assess part distortion (deflection and deformation) is to resort to high-precision 3D scanning and coordinate measurement systems. 3) For certain applications, a more dedicated penalization scheme can be developed for the topology optimization framework of a TPMS lattice if a smoother transition of the lattice gradient is to be sought.

Supporting Information

Supporting Information is available from the Wiley Online Library or from the author.

Acknowledgements

Conflict of Interest

The authors declare no conflict of interest.

Data Availability Statement

The data that support the findings of this study are available from the corresponding author upon reasonable request.

Keywords

[1] T. Grünberger, R. Domröse, *Laser Tech. J.* **2015**, *12*, 45.
[2] K. V. Wong, A. Hernandez, *ISRN Mech. Eng.* **2012**, *2012*, 208760.
[3] S. Bremen, W. Meiners, A. Diatlov, *Laser Tech. J.* **2012**, *9*, 33.
[4] L. Lü, J. Y. H. Fuh, Y. S. Wong, *Selective Laser Sintering*, Springer US, Boston, MA **2001**, pp. 89–142, ISBN 978-1-4615-1469-5.
[5] I. Yadroitsev, I. Yadroitsava, in *Fundamentals of Laser Powder Bed Fusion of Metals* (Eds: I. Yadroitsev, I. Yadroitsava, A. du Plessis, E. MacDonald), Additive Manufacturing Materials and Technologies, Elsevier, Amsterdam, Netherlands **2021**, pp. 39–77, ISBN 978-0-12-824090-8.
[6] Y.-H. Kuo, C.-C. Cheng, Y.-S. Lin, C.-H. San, *Struct. Multidiscip. Optim.* **2018**, *57*, 183.
[7] S. C. Subedi, A. Shahba, M. Thevamaran, D. J. Thoma, K. Suresh, *Addit. Manuf.* **2022**, *57*, 102956.
[8] J. Jiang, X. Xu, J. Stringer, *J. Manuf. Mater. Process.* **2018**, *2*, 64.
[9] K. Thrimurthulu, P. M. Pandey, N. Venkata Reddy, *Int. J. Mach. Tools Manuf.* **2004**, *44*, 585.
[10] P. Das, R. Chandran, R. Samant, S. Anand, *Procedia Manuf.* **2015**, *1*, 343, 43rd North American Manufacturing Research Conference, NAMRC 43, June 2015, UNC Charlotte, North Carolina, USA.
[11] L. Cheng, A. To, *Comput.-Aided Des.* **2019**, *113*, 1.
[12] T. Nancharaiah, in *Advances in Materials Processing and Manufacturing Applications* (Eds: A. Patnaik, E. Kozeschnik, V. Kukshal), Springer Singapore, Singapore **2021**, pp. 251–259, ISBN 978-981-16-0909-1.
[13] A. M. Mirzendehdel, K. Suresh, *Comput.-Aided Des.* **2016**, *81*, 1.
[14] M. Langelaar, *Addit. Manuf.* **2016**, *12*, 60.
[15] M. McConaha, V. Venugopal, S. Anand, *J. Manuf. Sci. Eng.* **2021**, *143*, 071001.
[16] S. Xu, J. Liu, Y. Ma, *Comput. Methods Appl. Mech. Eng.* **2022**, *389*, 114380.
[17] A. Takezawa, Q. Chen, A. C. To, *Addit. Manuf.* **2021**, *48*, 102422.
[18] M. Zhou, Y. Liu, Z. Lin, *Comput. Methods Appl. Mech. Eng.* **2019**, *353*, 24.
[19] T. Miki, S. Nishiwaki, *Finite Elem. Anal. Des.* **2022**, *203*, 103708.
[20] G. Allaire, M. Bihr, B. Bogosel, *Struct. Multidiscip. Optim.* **2020**, *61*, 2377.
[21] Z.-D. Zhang, O. Ibhadode, U. Ali, C. F. Dibia, P. Rahnama, A. Bonakdar, E. Toyserkani, *Int. J. Mech. Mater. Des.* **2020**, *16*, 897.
[22] L. Cheng, X. Liang, J. Bai, Q. Chen, J. Lemon, A. To, *Addit. Manuf.* **2019**, *27*, 290.
[23] J. Pellens, G. Lombaert, M. Michiels, T. Craeghs, M. Schevenels, *Struct. Multidiscip. Optim.* **2020**, *61*, 2291.
[24] K. Bartsch, F. Lange, M. Gralow, C. Emmelmann, *J. Laser Appl.* **2019**, *31*, 022302.
[25] Z. Sun, G. Vladimirov, E. Nikolaev, L. F. Velásquez-García, *J. Microelectromech. Syst.* **2018**, *27*, 1171.
[26] O. Ibhadode, Z. Zhang, J. Sixt, K. M. Nsiempba, J. Orakwe, A. Martinez-Marchese, O. Ero, S. I. Shahabad, A. Bonakdar, E. Toyserkani, *Virtual Phys. Prototyping* **2023**, *18*, 2181192.
[27] H. Mohammadtaheri, R. Sedaghati, M. Molavi-Zarandi, *Int. J. Adv. Manuf. Technol.* **2022**, *122*, 2187.
[28] E. Andreassen, C. S. Andreasen, *Comput. Mater. Sci.* **2014**, *83*, 488.
[29] S. Arabnejad, D. Pasini, *Int. J. Mech. Sci.* **2013**, *77*, 249.
[30] O. Al-Ketan, R. K. Abu Al-Rub, *Adv. Eng. Mater.* **2019**, *21*, 1900524.
[31] O. Al-Ketan, R. Rowshan, R. K. Abu Al-Rub, *Addit. Manuf.* **2018**, *19*, 167.
[32] D. Li, N. Dai, Y. Tang, G. Dong, Y. F. Zhao, *J. Mech. Des.* **2019**, *141*, 7.
[33] X. Wu, D. Ma, P. Eisenlohr, D. Raabe, H.-O. Fabritius, *Bioinspiration Biomimetics* **2016**, *11*, 045001.
[34] S. Khaderi, V. Deshpande, N. Fleck, *Int. J. Solids Struct.* **2014**, *51*, 3866.
[35] D. Li, W. Liao, N. Dai, G. Dong, Y. Tang, Y. M. Xie, *Comput.-Aided Des.* **2018**, *104*, 87.
[36] S. Rastegarzadeh, J. Wang, J. Huang, in *ASME 2021 Int. Design Engineering Technical Conf. Computers and Information in Engineering Conf., Volume 2: 41st Computers and Information in Engineering Conf. (CIE)*, New York, USA **2021**, p. V002T02A046, https://doi.org/10.1115/DETC2021-71980.
[37] X. Liang, W. Dong, S. Hinnebusch, Q. Chen, H. T. Tran, J. Lemon, L. Cheng, Z. Zhou, D. Hayduke, A. C. To, *Addit. Manuf.* **2020**, *32*, 101091.
[38] M. P. Bendsøe, *Struct. Optim.* **1989**, *1*, 193.
[39] M. Zhou, G. I. N. Rozvany, *Comput. Methods Appl. Mech. Eng.* **1991**, *89*, 309.
[40] M. P. Bendsøe, O. Sigmund, *Arch. Appl. Mech.* **1999**, *69*, 635.
[41] Y. M. Xie, G. P. Steven, *Comput. Struct.* **1993**, *49*, 885.
[42] S. Osher, J. A. Sethian, *J. Comput. Phys.* **1988**, *79*, 12.
[43] J. A. Sethian, *Level Set Methods and Fast Marching Methods: Evolving Interfaces in Computational Geometry, Fluid Mechanics, Computer Vision, and Materials Science*, Vol. 3, Cambridge University Press, Cambridge, England **1999**.
[44] G. Allaire, F. Jouve, A.-M. Toader, *C. R. Math.* **2002**, *334*, 1125.
[45] M. Y. Wang, X. Wang, D. Guo, *Comput. Methods Appl. Mech. Eng.* **2003**, *192*, 227.
[46] H. A. Eschenauer, V. V. Kobelev, A. Schumacher, *Struct. Optim.* **1994**, *8*, 42.
[47] J. Sokolowski, A. Zochowski, *SIAM J. Control Optim.* **1999**, *37*, 1251.
[48] M. Wallin, M. Ristinmaa, H. Askfelt, *Struct. Multidiscip. Optim.* **2012**, *45*, 171.

**ADVANCED
SCIENCE NEWS**

www.advancedsciencenews.com

**ADVANCED
ENGINEERING
MATERIALS**

www.aem-journal.com

[49] M. Wang, S. Zhou, *CMES Comput. Model. Eng. Sci.* **2004**, *6*, 373.

[50] M. Burger, R. Stainko, *SIAM J. Control Optim.* **2006**, *45*, 1447.

[51] I. Maskery, L. A. Parry, D. Padrão, R. J. M. Hague, I. A. Ashcroft, *Addit. Manuf.* **2022**, *49*, 102510.

[52] K. Svanberg, *Int. J. Numer. Methods Eng.* **1987**, *24*, 359.

[53] O. Sigmund, *Struct. Multidiscip. Optim.* **2007**, *33*, 401.

[54] E. Andreassen, A. Clausen, M. Schevenels, B. S. Lazarov, O. Sigmund, *Struct. Multidiscip. Optim.* **2011**, *43*, 1.

2300976 (9 of 9)